energies

MDPI

Article

A Modified Resonant Column Device for In-Depth Analysis of Vibration in Cohesive and Cohesionless Soils

Piotr E. Srokosz, Ireneusz Dyka, Marcin Bujko and Marta Bocheńska *

Faculty of Geoengineering, University of Warmia and Mazury in Olsztyn, 10-720 Olsztyn, Poland; psrok@uwm.edu.pl (P.E.S.); i.dyka@uwm.edu.pl (I.D.); marcin.bujko@uwm.edu.pl (M.B.)
* Correspondence: marta.baginska@uwm.edu.pl

Abstract: With the accelerating progression of global climate change, switching to renewable energy sources is inevitable. Wind energy is a fast-growing branch of this industry, and according to the 2021 Global Wind Report, this trend must continue in order to limit the increase in global average temperature. While onshore wind turbines still dominate and account for most recent growth, offshore wind turbines are becoming a promising alternative for geographical, power density-related or even aesthetic reasons. Offshore wind turbines are subjected to more complex loading conditions and proper foundation design is very challenging, however, this is crucial for ensuring and maintaining the structure's reliability. Soil dynamic tests are one of the bases for wind turbine foundation design. Technical regulations in many countries require such tests to be carried out in a Resonant Column (RC). In this study, a modification of the RC sensors and data acquisition system was introduced in order to conduct in-depth analysis of vibrating soil specimens. The new set of sensors contained five additional accelerometers (Analog Devices ADXL345) attached to the surface of a soil specimen that was subjected to dynamic loading. These accelerometers sent the data to a new data acquisition system, an ARM microcontroller with software developed by authors. The software was able to process test results synchronously with the original software of the RC device. Additionally, the load control system was supplemented with a current pulse generator, which makes it possible to observe the propagation of high-frequency mechanical waves in the tested materials. The modified dynamic testing equipment allowed for the measuring of accelerations and displacements at specific selected points located along the height of the sample, with sampling frequency more than three times higher than that offered by the sensors originally built into the RC device. As a result, some additional dynamic phenomena (i.e., disturbances in the uniformity of vibrations of non-cohesive materials, specimen–device contact imperfections) were observed in the tested soil specimens which remained undetected in standard RC test.

Keywords: ground vibrations; offshore wind turbines; foundations; soil dynamic testing; resonant column

check for updates

Citation: Srokosz, P.E.; Dyka, I.; Bujko, M.; Bocheńska, M. A Modified Resonant Column Device for In-Depth Analysis of Vibration in Cohesive and Cohesionless Soils. *Energies* **2021**, *14*, 6647. https://doi.org/10.3390/en14206647

Academic Editor: Waldemar Korzeniowski

Received: 29 August 2021
Accepted: 8 October 2021
Published: 14 October 2021

Publisher's Note: MDPI stays neutral with regard to jurisdictional claims in published maps and institutional affiliations.

Copyright: © 2021 by the authors. Licensee MDPI, Basel, Switzerland. This article is an open access article distributed under the terms and conditions of the Creative Commons Attribution (CC BY) license (https://creativecommons.org/licenses/by/4.0/).

1. Introduction

As global climate change progresses, switching to low-carbon energy sources becomes one of the most urgent challenges society is currently facing. Recently, the sense of urgency has been increasing as countries and regions strive to reach net zero CO_2 emissions and limit global average temperature increase to no more than 1.5 °C. The use of wind energy is a powerful alternative to burning fossil fuels. According to the latest Global Wind Report [1] the year 2020 set a new record with 53% year-to-year growth of global wind industry. In 2020, 93 GW of wind power was installed despite all the challenges of the global pandemic, which shows that the wind industry is very resilient. The new installations bring global cumulative wind power capacity up to 743 GW. However, the report also shows that despite reaching a record in terms of new wind capacity, progress is still far from the desired levels. In order to meet the criteria set by the Intergovernmental Panel on Climate Change, around 180 GW needs to be installed per year.

In the wind industry onshore wind power plants still dominate, accounting for over 90% of the aforementioned growth. However, considering their constantly growing size onshore wind turbines often give rise to objections (e.g., aesthetic reasons). Further challenges arise when the largest wind resources are located far from high-demand regions. Therefore, a tendency to place wind turbines offshore has become apparent; according to the recent IRENA report [2], in 2020 offshore wind increased to around 5% of total wind capacity.

Although the wind power density is higher in offshore areas [3], the offshore wind turbines design process can be a more challenging task due to the complex loading conditions caused by a combination of wind, waves and sometimes ice. According to [4,5], in extreme conditions lateral loading can account for as much as 60% of the vertical load, and the biggest challenge for the foundation is to bear large and repetitive lateral loads [6]. The cyclic loading and dynamic effects that occur in such conditions have to be considered in the design process.

Proper foundation design is crucial for any structure's reliability; however, economic efficiency in foundation design is an equally important matter. Considering investment per megawatt (MW), offshore wind turbine installation is still about 50% more costly compared to onshore installation [7]. The foundation of the wind turbine can account for as much as 15% of the installed cost [7]. However, while the turbines are about 20% more expensive, the towers and foundations can cost 350% more than similar onshore parts [7]. Considering this, precise and reliable geotechnical calculations can generate substantial savings. The cyclic or dynamic loading experimental database is growing, however, data are still very limited. There is therefore a great need for research in this area.

The most common offshore wind turbine substructures are monopile [7–9], gravity based foundation [10,11], tripod foundation [12–14], jacket foundation [15–17], suction bucket [18–20], floating foundation [21–23] and hybrid structures [24–27]. A full review of offshore wind turbine substructures and some design recommendations can be found, e.g., in [7,28,29].

The dynamics of wind turbines were analyzed, e.g., in [30]. In this study, monopile and gravity base wind turbine foundations were subjected to free vibration. The authors investigated the potential problem of resonance and resulting failure of offshore wind turbines. The natural frequency analysis of soil–foundation systems showed that special attention should be paid to the interaction of soil and structure.

Many of the recent studies focus on the analysis of soil–structure interaction (SSI) [31–34] or soil-structure-wave interaction [11].

Particular attention should be paid to soil stiffness and how it changes during the structure's lifetime. It was discovered in [35] that soil stiffness degradation can disturb the dynamic stability of an offshore wind turbine on a monopile foundation. The percentage change in the natural frequency of soil relative to the percentage change in soil stiffness is presented in Figure 1. It can be seen that a 40% change in soil stiffness resulted in a 1% change in natural frequency. In [35], the authors recommend conducting soil tests in a resonant column for reliable prediction of the long-term behavior of monopile foundations.

The aforementioned studies show that special attention should be paid to the determination of soil stiffness parameters during the offshore wind turbine design process. Moreover, soil stiffness evolution during the structure's lifetime plays a very important role in the whole structure's reliability. Foundation design cannot be optimal without a proper understanding of soil behavior and its changes over time. Moreover, standard laboratory testing devices can sometimes be insufficient to analyze the nature of mechanical phenomena. For example, in [36] additional measurement methods had to be introduced to the standard Torsional Shear (TS) test in order to observe the actual displacement distribution along the specimen subjected to torsional shearing. In the standard testing procedure, the horizontal displacement distribution is assumed to be linear along the specimen's height. The Scale Invariant Feature Transform (SIFT) optical flow method showed that for small strains one of the most important stiffness parameters of soil, the shear modulus or G, is determined with a non-negligible error [36].

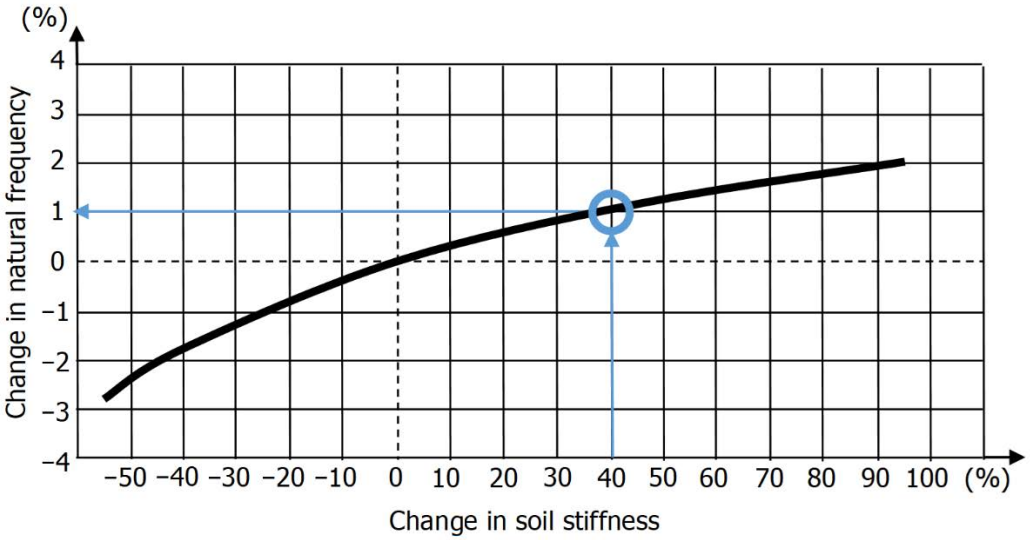

Figure 1. Natural frequency change due to change in soil stiffness during the lifetime of an offshore wind turbine with monopile foundation [35].

As accurate estimation of soil stiffness parameters is crucial for optimal foundation design, the main focus of this study was to conduct a more in-depth analysis of dynamic tests of soil specimens. For this purpose, a Resonant Column/Torsional Shearing (RC/TS) device was modified. Five additional accelerometers were attached to the soil specimen's surface to perform more accurate analysis of the specimen subjected to vibration. The accelerometers were attached directly to the specimen and not to the elements of testing equipment, as was the case in the original version of the device. To complement the RC tests, an additional single impulse method was proposed.

2. Materials and Methods

2.1. Soil Parameters

According to the ISO 14688-1:2002 [37] standard, the materials used in this study can be classified as sand (Sa) and sandy-clayey silt (saclSi). All samples consisted of factions with particle sizes in the range of 0.0004–4.0 mm. All sand specimens were prepared using mixtures of dry gravel (Gr, >2.0 mm) and coarse (CSa, 0.63–2.0 mm), medium (MSa, 0.2–0.63 mm), and fine (FSa, 0.063–0.2 mm) grained silica sand. Cohesive specimens consisted mainly of silty (Si, 0.002–0.063 mm) and clayey factions (Cl, <0.002 mm). The parameters of the tested soils are given in Table 1. Sand with these specific characteristics was chosen for the experiments based on the analysis performed by Wichtmann [38], who carried out about 650 RC tests with additional measurement of the pressure wave (P-wave) speed. In his study, incohesive soils of 65 different grain size distributions were tested and analyzed. Grain shapes are presented in Figure 2; Figure 3 shows the grain size distribution of the tested material.

Table 1. Parameters of the tested soil *.

Soil Type	G_s [-]	d_{50} [mm]	d_{60} [mm]	d_{10} [mm]	C_U [-]	e [-]	ρ [g/cm^3]
Silica sand 3	2.65	0.33	0.48	0.12	4.0	0.37	1.93
saclSi 1	2.66	0.013	0.0275	0.00125	22.0	0.27	2.09

* d, d_{60}, d_{10}—the values of the particle diameter at 50%, 60% and 10% in the cumulative distribution; e—void ratio, C_U—uniformity coefficient, ρ—soil density, G_s—specific gravity.

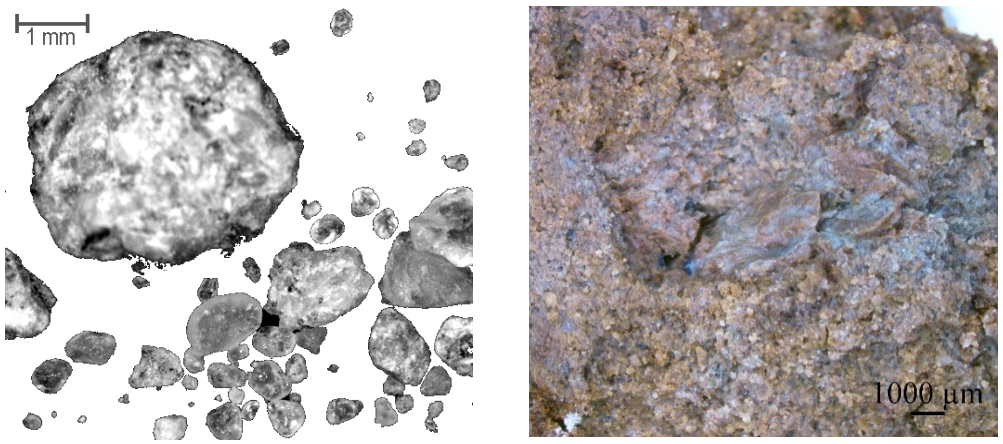

Figure 2. Tested soils in magnification; (**a**) Grains of Sand 3 in magnification (data from [39]); (**b**) Grains of the saclSi soil in magnification (the sample's cross-section).

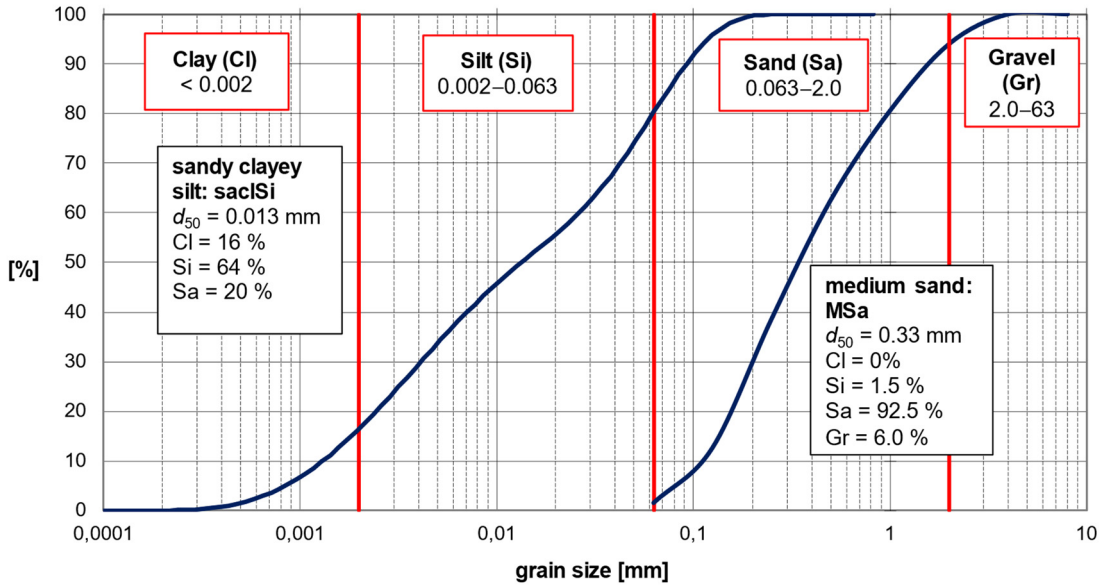

Figure 3. Grain size distribution of the tested soils.

2.2. Resonant Column/Torsional Shear (RC/TS) Device

The laboratory experiments were conducted using an RC/TS (Resonant Column/Torsional Shearing) apparatus (Wykeham Farrance model WF8500). The device is commonly used in geotechnical laboratories for determining soil stiffness parameters and dynamic properties, such as the shear modulus G and the damping ratio D. Figure 4 presents the components of the RC/TS device. A cylindrically shaped soil specimen is placed on the porous stone (i.e., fixed at the bottom end). A cyclic torsional loading is applied to the upper end of the specimen (amplitude, frequency and number of cycles depend on the specific type of test to be performed). The drive system is the rotor Nd-FeB magnet (alloy of neodymium, iron, and boron, $Nd_2Fe_{14}B$) and the stator coils. The specimen is covered with a latex membrane that separates the soil from the water in the internal polycarbonate cylinder. The pressure inside the internal cylinder can be set to a specific value to simulate the pressure conditions in natural ground. The acceleration and displacements of the specimen are measured near the upper end of the specimen (the accelerometer and the proximity sensors, see Figure 4). The specimen and the measurement system are placed inside an external polycarbonate cylinder filled with compressed air.

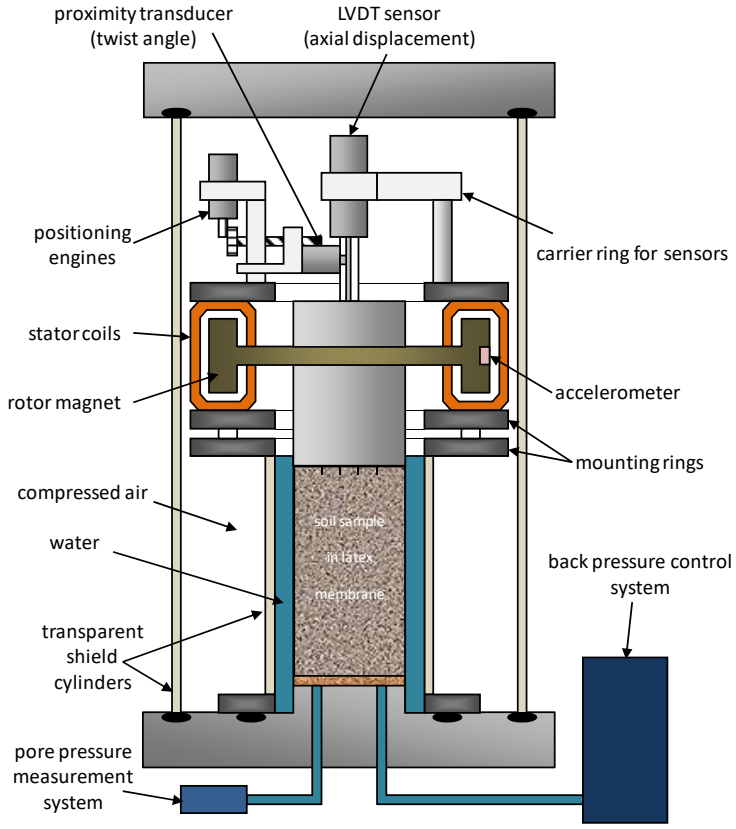

Figure 4. Components of RC/TS apparatus [40].

The device has several testing modes that enable performing different types of soil tests.

1. Torsional Shearing (TS) mode
2. Resonant Column (RC) mode
3. Free Decay (FD) mode

In the TS mode the specimen is subjected to a harmonically changing torque T of an amplitude T_0 and the twist angle φ is measured. The cyclic load frequency f is 0–50 Hz (the loading can be considered as cyclic slow-changing, not dynamic). Based on the torque and the corresponding twist angle the tangential stress and shear strain are calculated. The obtained stress–strain relationship allows estimation of the shear modulus G.

Soil testing in the RC mode allows determination of the resonant frequency f_r of the soil specimen as well as the damping ratio D. During the RC test the specimen is being dynamically loaded with different torque frequencies which change within the range of 0–300 Hz. The resonant frequency corresponds to the maximum twist angle and is identified based on the resulting graph (see for example Figure 5).

Using RC mode, the shear modulus G can also be determined through further analysis. The interpretation of results is based on the relationship between the specimen's natural frequency and the velocity of the transverse elastic wave through the soil. The resonant frequency corresponds to the maximum twist angle, and the shear modulus G is related to the resonant frequency of the specimen.

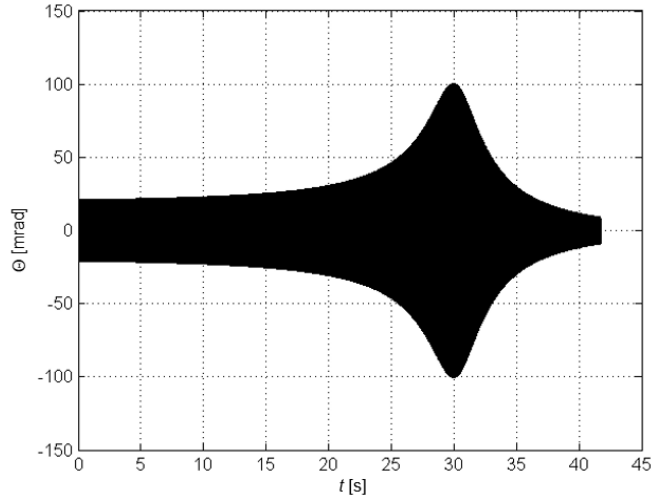

Figure 5. The RC test results for frequency spectrum 25–200 Hz, viscous damping constant $C = 0.1C_{cr}\left[\frac{\mathrm{N{\cdot}m{\cdot}s}}{\mathrm{rad}}\right]$ (C_{cr}—critical damping), moment of inertia of the drive system $I_0 = 10^{-6}\left[\mathrm{kg}{\cdot}\frac{\mathrm{m}^2}{\mathrm{rad}}\right]$, torsional elastic constant $K = 0.5\left[\frac{\mathrm{N{\cdot}m}}{\mathrm{rad}}\right]$.

The RC test is done in the following steps [40]

1. The amplitude of vibration $A(t, \omega)$ is measured in a given frequency spectrum.
2. The measured data is transformed using the Fast Fourier Transform (FFT) method, $FFT(A)$. The signal is presented as a function of frequency (compare Figures 5 and 6).
3. The resonant frequency f_r of the specimen is equal to the frequency for which $FFT(A)$ attains its maximum.
4. The *half-power bandwidth* $(f_1; f_2)$ is the frequency range in which half of the vibrating system's power is dissipated. It is given by frequencies for which the value of $FFT(A)$ is $\left(\frac{\max(FFT(A))}{\sqrt{2}}; \max(FFT(A))\right)$
5. The damping ratio D can be calculated with the formula $D = \frac{f_2 - f_1}{2f_r}$.

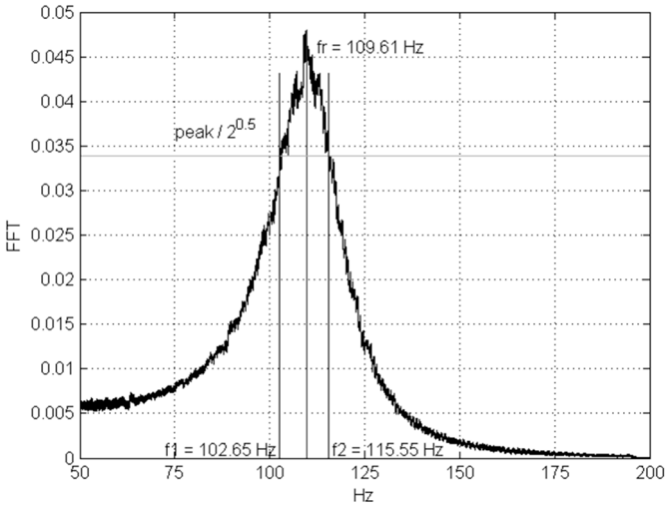

Figure 6. The FFT analysis of RC data (in Figure 5). Identification of the half-power bandwidth.

The damping ratio can be also determined using the FD mode. In this mode, initially applied impulse torque causes free damped vibration of the specimen (Figure 7). The FD test is used for determining the damping ratio D. It can be done by comparing the

subsequent periods of oscillation. The subsequent rotation amplitudes $\Theta_1, \Theta_2, \Theta_3, \ldots, \Theta_i$ are measured during the test and then compared together

$$\frac{\Theta_1}{\Theta_2} \approx \frac{\Theta_2}{\Theta_3} \approx \frac{\Theta_3}{\Theta_4} \approx \ldots \approx \frac{\Theta_{i-1}}{\Theta_i} = e^{\delta} \tag{1}$$

to determine the logarithmic decrement of damping δ. The damping ratio can be calculated with the following formula

$$D = \frac{\delta}{\sqrt{4\pi^2 + \delta^2}}. \tag{2}$$

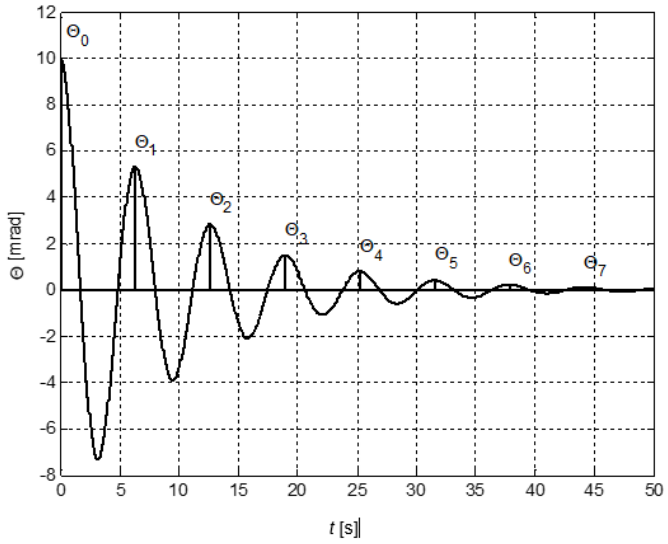

Figure 7. Subsequent rotation amplitudes in FD mode for actual viscous damping $C = 0.1C_{cr}$ $\left[\frac{\text{N·m·s}}{\text{rad}}\right]$ (critical damping), moment of inertia of the drive system $I_0 = 0.001$ $\left[\text{kg}\cdot\frac{\text{m}^2}{\text{rad}}\right]$, torsional elastic constant $K = 0.001\left[\frac{\text{N·m}}{\text{rad}}\right]$, maximum amplitude $\Theta_0 = 0.01$ [rad].

The non-negative form of the solution is assumed, because δ is always non-negative.

For a more detailed description and the theoretical basis of the TS, RC and FD tests see [40].

2.3. Modified RC/TS Device

In order to perform more in-depth analysis of the dynamic tests, that is, the RC and FD testing modes, we introduced modifications to the original device. The measurement system was made of three main components (Figure 8)

1. A set of five accelerometers (Analog Devices ADXL345) attached to the specimen surface along a vertical line (see Figure 9)
2. A control and data acquisition system (NXP LPC2106)
3. Software for supervision and experimental data processing (Research Supervision System v.5, RSS.5)

The ADXL345 accelerometer used was a microelectric mechanical system (MEMS) that could measure acceleration along three perpendicular directions. It enabled measurement in ranges from ±2 g to ±16 g, with 4 mg resolution. The supply voltage range was 3 V to 5 V, thanks to a voltage stabilizer on the printed circuit board. The sensor communicated with the controller via Serial Peripheral Interface (SPI) bus with a maximum clock rate of 5 MHz. The measuring frequency was 3200 Hz and the measurements from all five sensors were time synchronized. It should be emphasized that the ADXL accelerometers could provide measurements with a sampling frequency over three times higher than the original

built-in accelerometer. This allowed for the observation of dynamic phenomena not only at selected points of the tested sample, but also with a much greater temporal resolution.

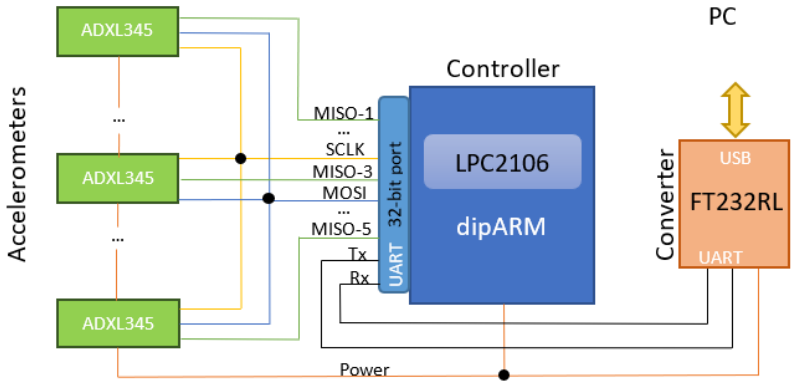

Figure 8. A schematic diagram of the measurement system architecture.

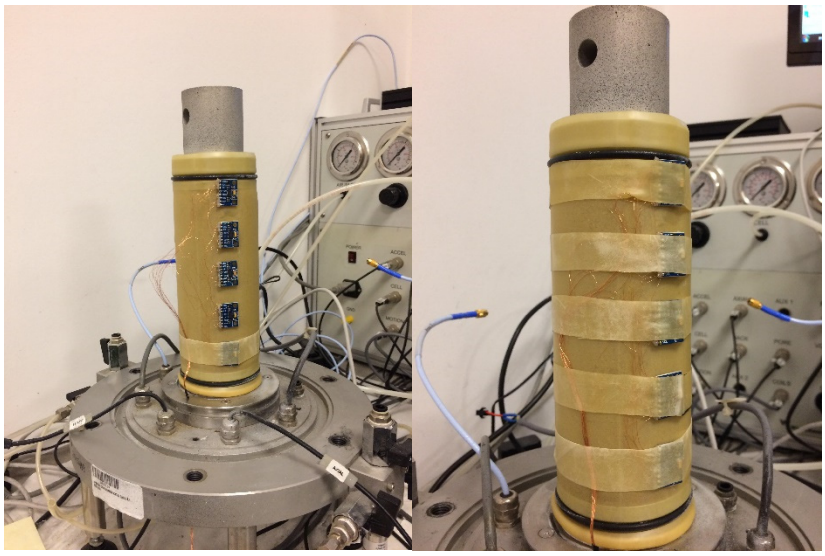

(**a**) (**b**)

Figure 9. Experimental setup: (**a**) Modified RC device with five accelerometers attached to the membrane on the specimen surface; (**b**) The accelerometers were stabilized with elastic bands.

The main component of the control and data acquisition system was a 32-bit microcontroller LPC2106 with a CPU of the ARM7TDMI-S architecture type. There were also two voltage stabilizers LDO (1.8 V and 3.3 V) on the PCB to ensure an acceptable voltage supply for the microcontroller. The LPC2106 used a 48 MHz clock signal which ensured data transmission through a universal asynchronous receiver-transmitter (UART) with a rate of 3 Mbaud. The microcontroller executed the batch file code from ROM written in C programming language. The code was a looped sequence of commands to control the ADXL345 measurements and supervise data transmission. Data were obtained cyclically and transmitted to the PC via UART-USB converter (FTDI FT232RL).

The Research Supervision System was based on Pascal programming language (Delphi) to provides a user interface for setting the measurement parameters (e.g., the measurement time, from 1 s to 30 s). Figure 10 presents the application windows.

The modified equipment was verified by comparing the results with the original device. The results obtained with the Resonant Column with additional accelerometers confirmed that the amplitude of vibration is proportional to the distance from the vibration source (measured along the specimen's height). This confirmed the theoretical predic-

tions used as a basis for the description and interpretation of the RC results. However, it was still possible that during the dynamic test some wave interactions (refraction and interference) could have occurred and affected the measurements. To investigate that assumption, the next experiment was conducted using a unit impulse (Dirac delta function) technique, instead of the RC chirp. The measurement system was made of three components (Figure 11).

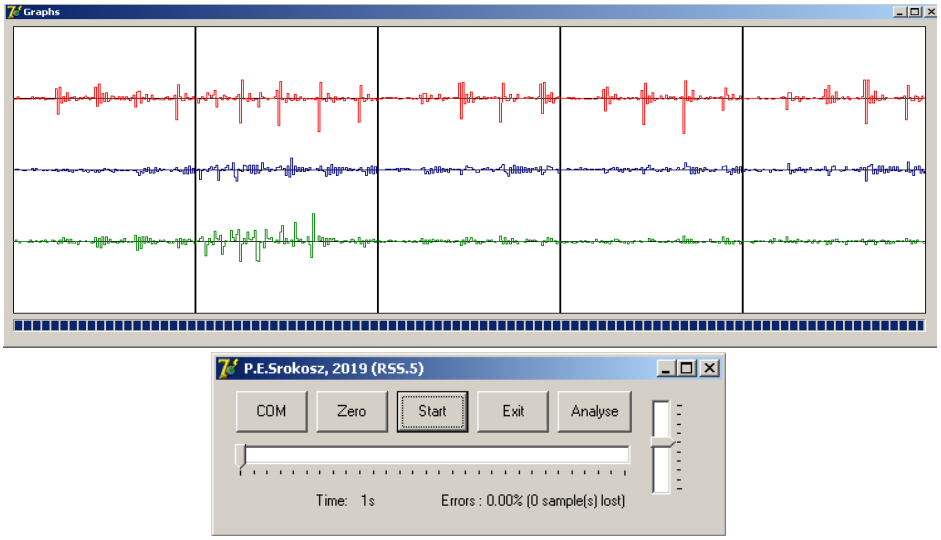

Figure 10. The Research Supervision System application windows.

1. An impulse generator
2. A system for acquisition of generated impulse parameters
3. Software for supervision and data acquisition

The generator consisted of a microcontroller to control the shape of the impulses (8-bit AVR) and a system to control the voltage amplitude and pulse triggering time. Generated voltage spectrum was the same as in the original driver in the RC device. The generator could be programmed directly through a built-in keyboard and an LCD screen. The parameters of the generated impulses could be precisely controlled thanks to the two-channel 12-bit analog-to-digital converter (ADC), which had a sampling frequency of 500 kHz. The microcontroller (8-bit AVR) controlled the ADC, taking measurements and providing data transmission to the PC through UART-USB (FTDI FT232RL). The microcontrollers from both modules executed the batch file code from ROM, written in C. The software for experiment supervision was based on Pascal programming language (Delphi) and provided a user interface for initializing measurements and saving the results. Figure 12 presents the application window.

2.4. Specimen Preparation

All sandy soil specimens were prepared in the following way. Firstly, a soil specimen was shaped in a latex membrane and in a rigid cylindrical form. The specimens were formed in five layers of material compacted with a hand rammer (about 25 strokes per layer). All of the tested specimens had the following dimensions: 140 mm (height) and 70 mm (diameter).

The clayey soil was sampled directly from the natural ground (in Olsztyn, Kortowo, Poland) in order to preserve the natural structure of an undisturbed soil sample. The soil was sampled from a depth of 6.10 m. Before the tests were conducted, the sample was stored in constant temperature and humidity in a hermetically sealed metal tube. The sample was extracted from the tube using a hydraulic piston, with special attention paid so as not to disturb the natural soil structure during this process. The sample was formed

to fit the required dimensions for the RC test, then installed on the porous stone (Figure 4) and covered with a latex membrane.

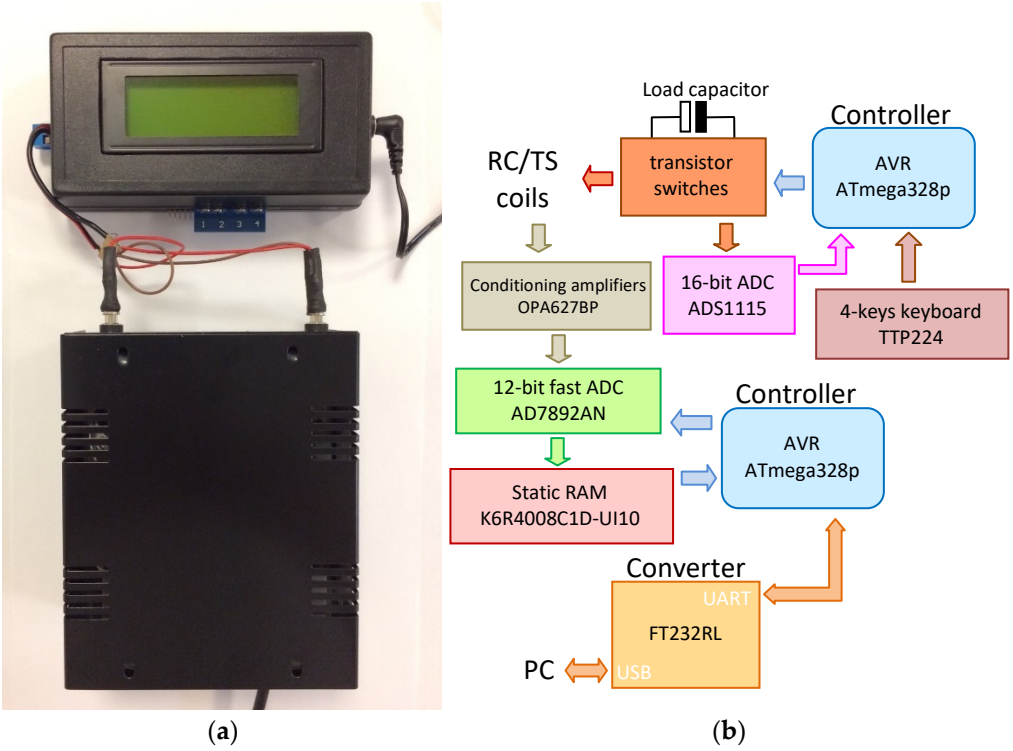

Figure 11. The control system and the measurement system: (**a**) Photograph; (**b**) Schematic diagram.

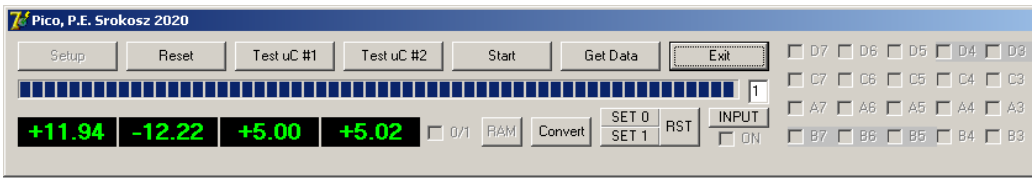

Figure 12. The application window of the software that controlled the parameters of the generated impulses.

After the specimen was installed, five ADXL accelerometers were glued to the latex membrane along a vertical line (see Figure 9a) and stabilized with elastic bands (Figure 9b). After that, the RC/TS device chamber equipment was assembled: the internal cylinder, drive system, measurement system, and external cylinder. The chamber was then pressurized for about 5 h to reconstitute the soil material (sand). During the tests performed in this study, the isotropic pressure was set to match the pressure conditions in the natural ground where the sand came from, as well as the pressure conditions at typical foundation depth.

The specimen was subjected to dynamic loading with a torque with a frequency changing within a specified spectrum in the RC test, and with a single impulse in the proposed second experiment. The tests were repeated for different torque amplitudes and different isotropic pressure values.

Weight and exact geometrical dimensions of the specimens were precisely measured during the experiment. To ensure that the mechanical features would be repeatable and reproducible, all of the specimens were prepared by the same person under the same laboratory conditions.

3. Results

In this section the standard RC tests results are compared with the results obtained with the additional accelerometers. In addition, the results of the single impulse tests

are presented. The colors in Figures 13–25 are assigned to the accelerometers in the following way.

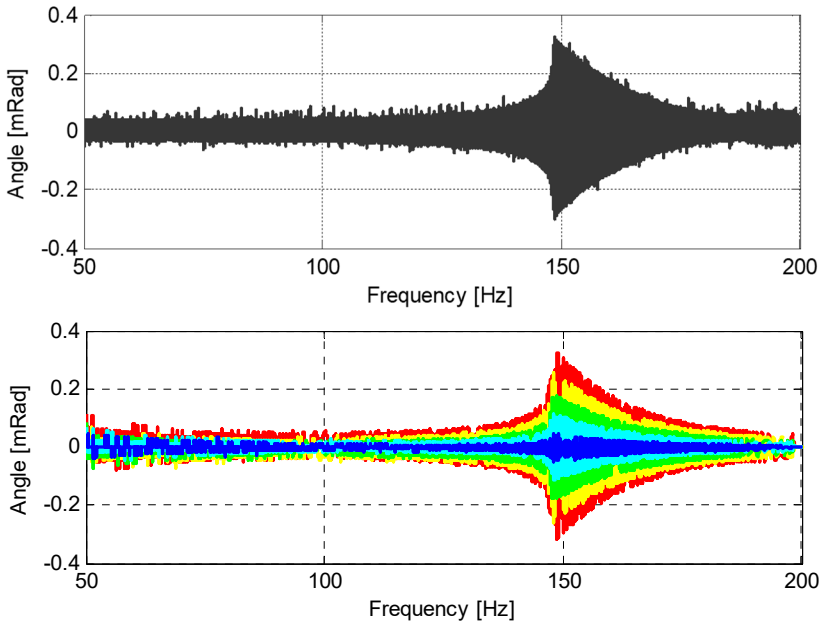

Figure 13. The results of RC testing. Standard RC test results are at the top; the results from the additional accelerometers are at the bottom. Material: Sand 3 (Sa); Isotropic pressure 50 kPa; Frequency spectrum 50–200 Hz; Excitation (torque) amplitude 0.5 V (– original built-in sensor, – the top sensor, S1, – the second sensor from the top, S2, – the third sensor from the top, S3, – the fourth sensor from the top, S4, – the bottom sensor, S5).

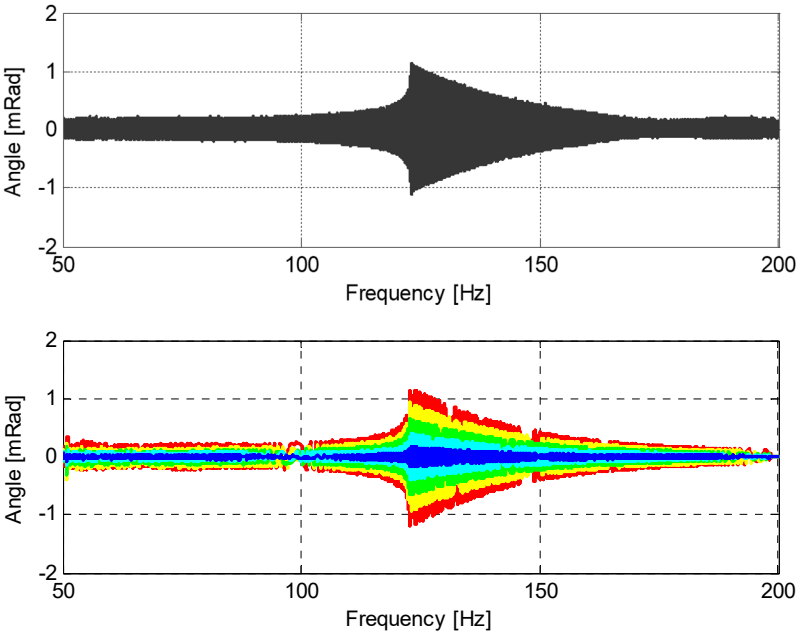

Figure 14. The results of RC testing. Standard RC test results are at the top; the results from the additional accelerometers are at the bottom. Material: Sand 3 (Sa); Isotropic pressure 50 kPa; Frequency spectrum 50–200 Hz; Excitation (torque) amplitude 2 V (– original built-in sensor, – the top sensor, S1, – the second sensor from the top, S2, – the third sensor from the top, S3, – the fourth sensor from the top, S4, – the bottom sensor, S5).

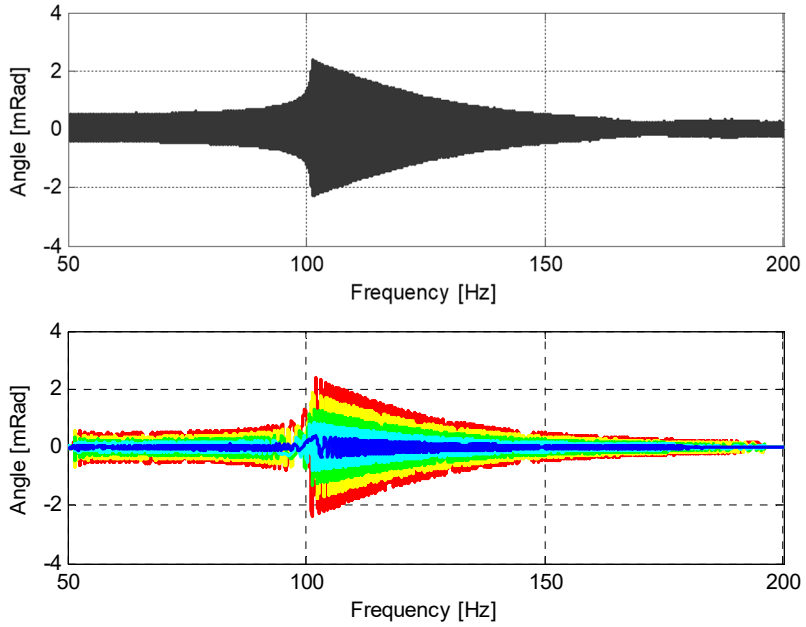

Figure 15. The results of RC testing. Standard RC test results are at the top; the results from the additional accelerometers are at the bottom. Material: Sand 3 (Sa); Isotropic pressure 50 kPa; Frequency spectrum 50–200 Hz; Excitation (torque) amplitude 4 V (– original built-in sensor, – the top sensor, S1, – the second sensor from the top, S2, – the third sensor from the top, S3, – the fourth sensor from the top, S4, – the bottom sensor, S5).

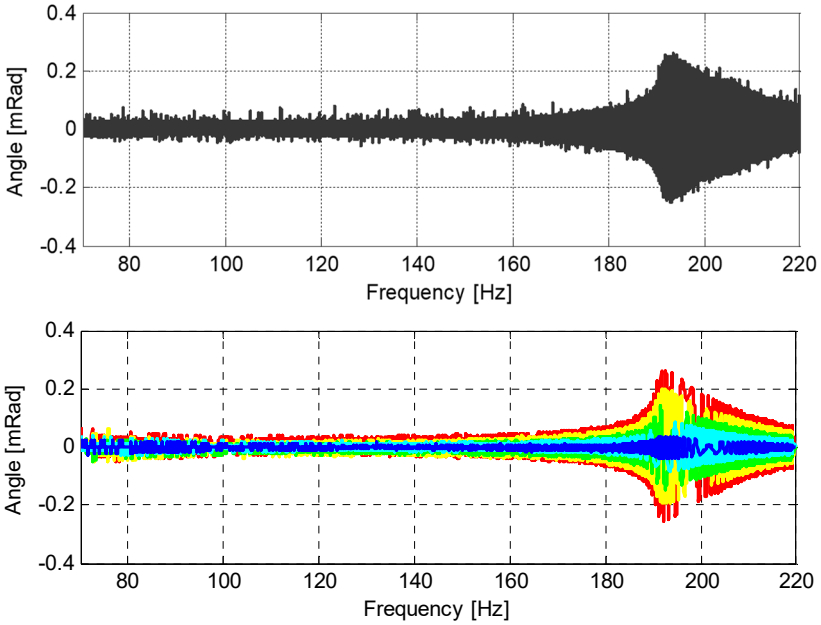

Figure 16. The results of RC testing. Standard RC test results are at the top; the results from the additional accelerometers are at the bottom. Material: Sand 3 (Sa); Isotropic pressure 100 kPa; Frequency spectrum 70–220 Hz; Excitation (torque) amplitude 0.5 V (– original built-in sensor, – the top sensor, S1, – the second sensor from the top, S2, – the third sensor from the top, S3, – the fourth sensor from the top, S4, – the bottom sensor, S5).

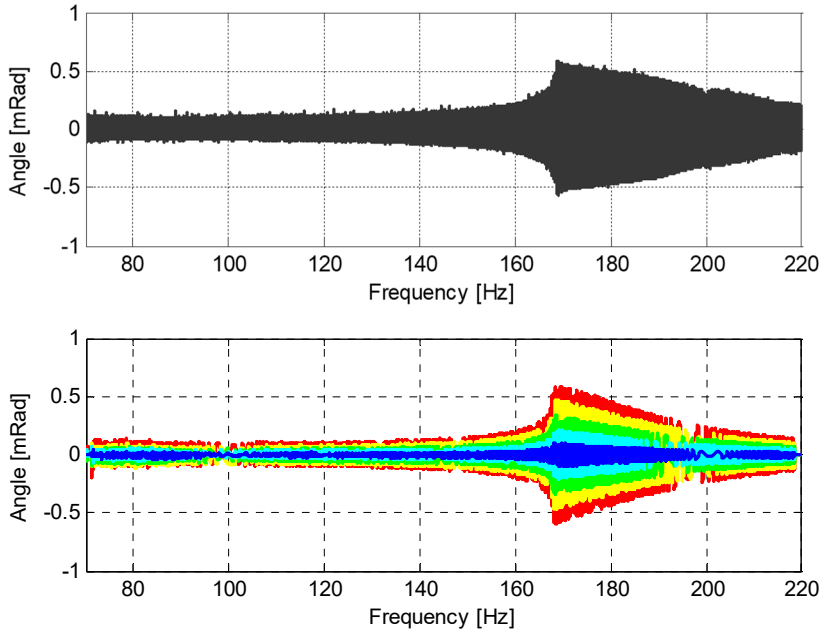

Figure 17. The results of RC testing. Standard RC test results are at the top; the results from the additional accelerometers are at the bottom. Material: Sand 3 (Sa); Isotropic pressure 100 kPa; Frequency spectrum 70–220 Hz; Excitation (torque) amplitude 2 V (– original built-in sensor, – the top sensor, S1, – the second sensor from the top, S2, – the third sensor from the top, S3, – the fourth sensor from the top, S4, – the bottom sensor, S5).

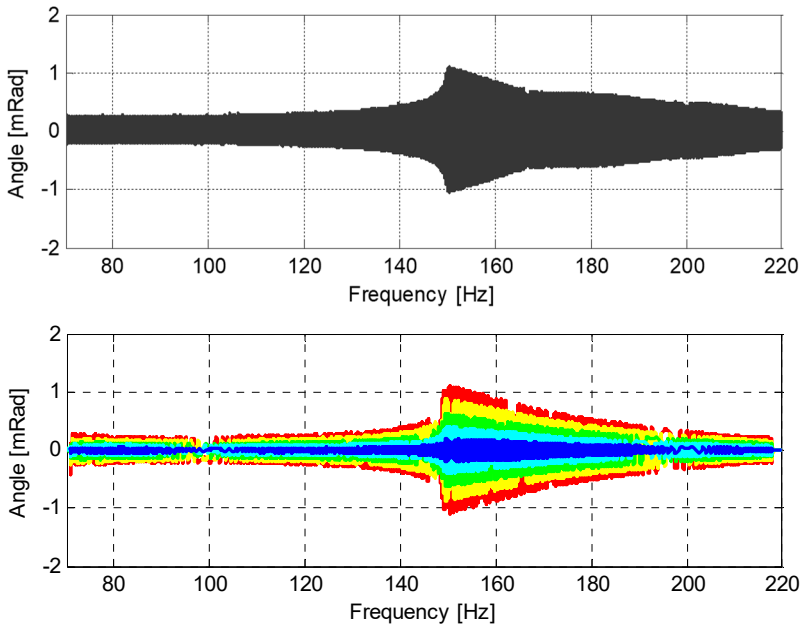

Figure 18. The results of RC testing. Standard RC test results are at the top; the results from the additional accelerometers are at the bottom. Material: Sand 3 (Sa); Isotropic pressure 100 kPa; Frequency spectrum 70–220 Hz; Excitation (torque) amplitude 4 V (– original built-in sensor, – the top sensor, S1, – the second sensor from the top, S2, – the third sensor from the top, S3, – the fourth sensor from the top, S4, – the bottom sensor, S5).

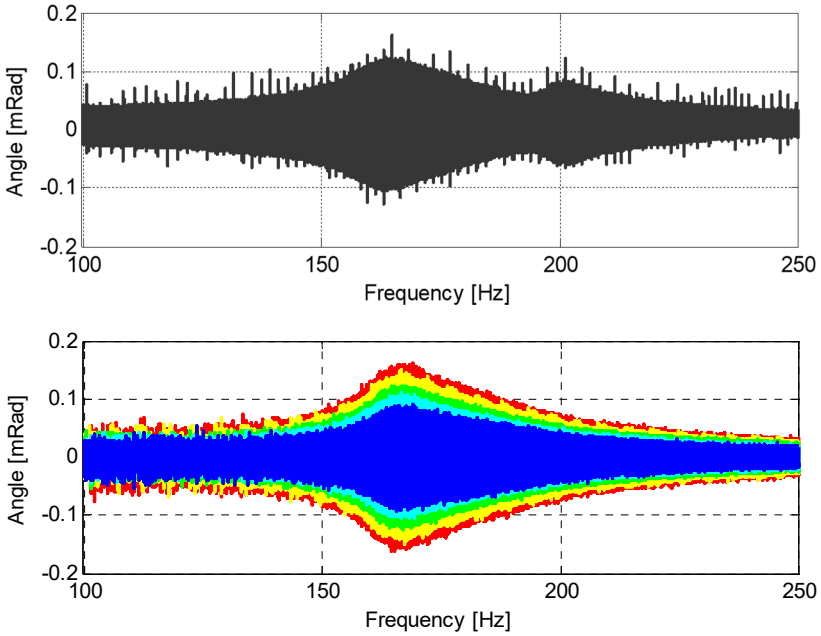

Figure 19. The results of RC testing. Standard RC test results are at the top; the results from the additional accelerometers are at the bottom. Material: saclSi 1; Isotropic pressure 50 kPa; Frequency spectrum 100–250 Hz; Excitation (torque) amplitude 0.5 V (– original built-in sensor, – the top sensor, S1, – the second sensor from the top, S2, – the third sensor from the top, S3, – the fourth sensor from the top, S4, – the bottom sensor, S5).

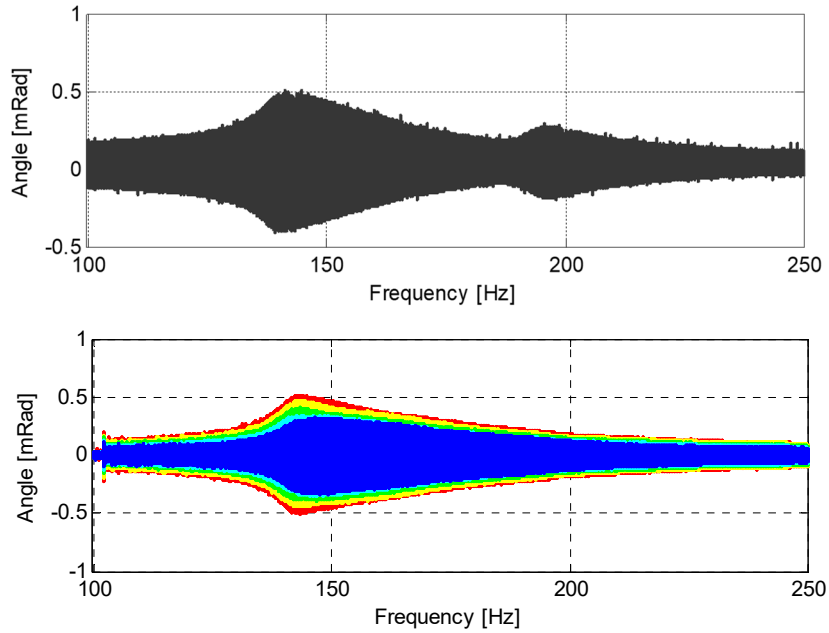

Figure 20. The results of RC testing. Standard RC test results are at the top; the results from the additional accelerometers are at the bottom. Material: saclSi 1; Isotropic pressure 50 kPa; Frequency spectrum 100–250 Hz; Excitation (torque) amplitude 2 V (– original built-in sensor, – the top sensor, S1, – the second sensor from the top, S2, – the third sensor from the top, S3, – the fourth sensor from the top, S4, – the bottom sensor, S5).

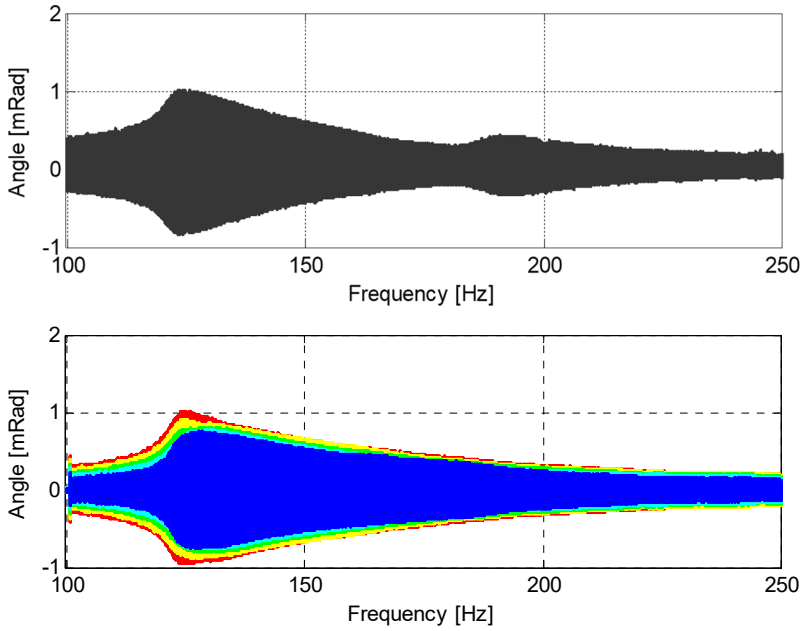

Figure 21. The results of RC testing. Standard RC test results are at the top; the results from the additional accelerometers are at the bottom. Material: saclSi 1; Isotropic pressure 50 kPa; Frequency spectrum 100–250 Hz; Excitation (torque) amplitude 4 V (– original built-in sensor, – the top sensor, S1, – the second sensor from the top, S2, – the third sensor from the top, S3, – the fourth sensor from the top, S4, – the bottom sensor, S5).

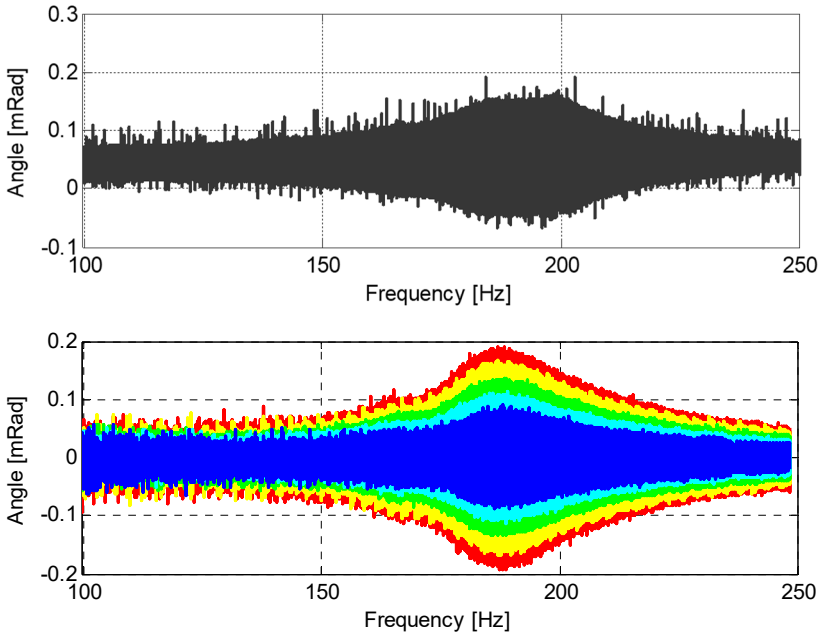

Figure 22. The results of RC testing. Standard RC test results are at the top; the results from the additional accelerometers are at the bottom. Material: saclSi 1; Isotropic pressure 100 kPa; Frequency spectrum 100–250 Hz; Excitation (torque) amplitude 0.5 V (– original built-in sensor, – the top sensor, S1, – the second sensor from the top, S2, – the third sensor from the top, S3, – the fourth sensor from the top, S4, – the bottom sensor, S5).

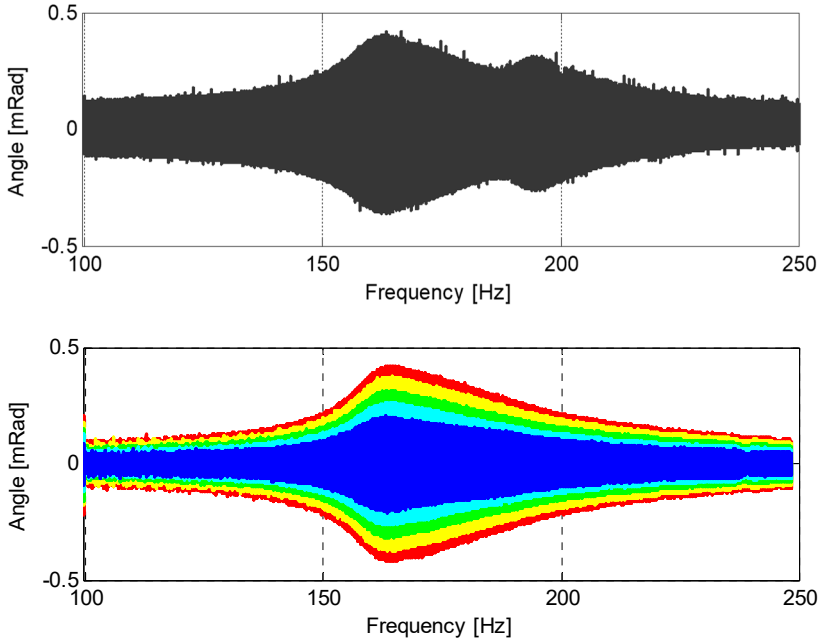

Figure 23. The results of RC testing. Standard RC test results are at the top; the results from the additional accelerometers are at the bottom. Material: saclSi 1; Isotropic pressure 100 kPa; Frequency spectrum 100–250 Hz; Excitation (torque) amplitude 2 V (– original built-in sensor, – the top sensor, S1, – the second sensor from the top, S2, – the third sensor from the top, S3, – the fourth sensor from the top, S4, – the bottom sensor, S5).

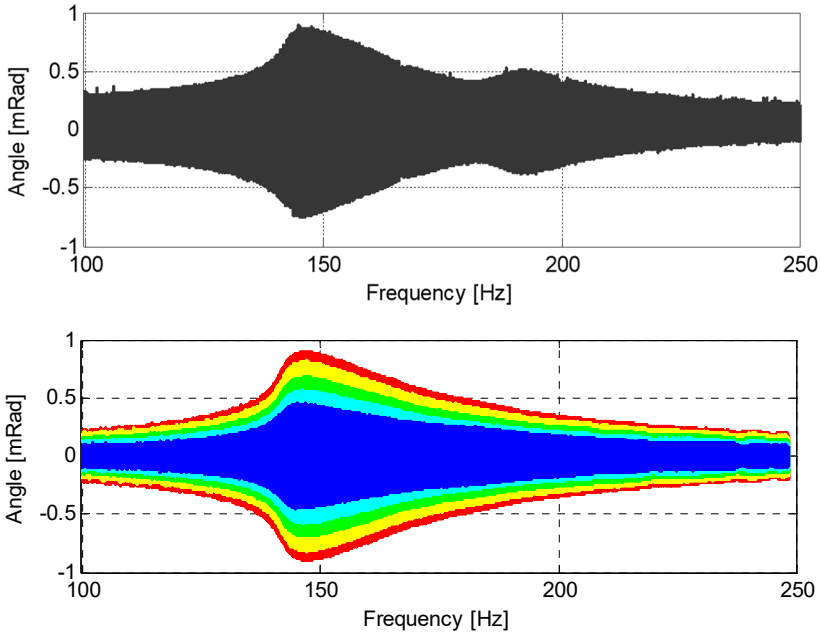

Figure 24. The results of RC testing. Standard RC test results are at the top; the results from the additional accelerometers are at the bottom. Material: saclSi 1; Isotropic pressure 100 kPa; Frequency spectrum 100–250 Hz; Excitation (torque) amplitude 4 V (– original built-in sensor, – the top sensor, S1, – the second sensor from the top, S2, – the third sensor from the top, S3, – the fourth sensor from the top, S4, – the bottom sensor, S5).

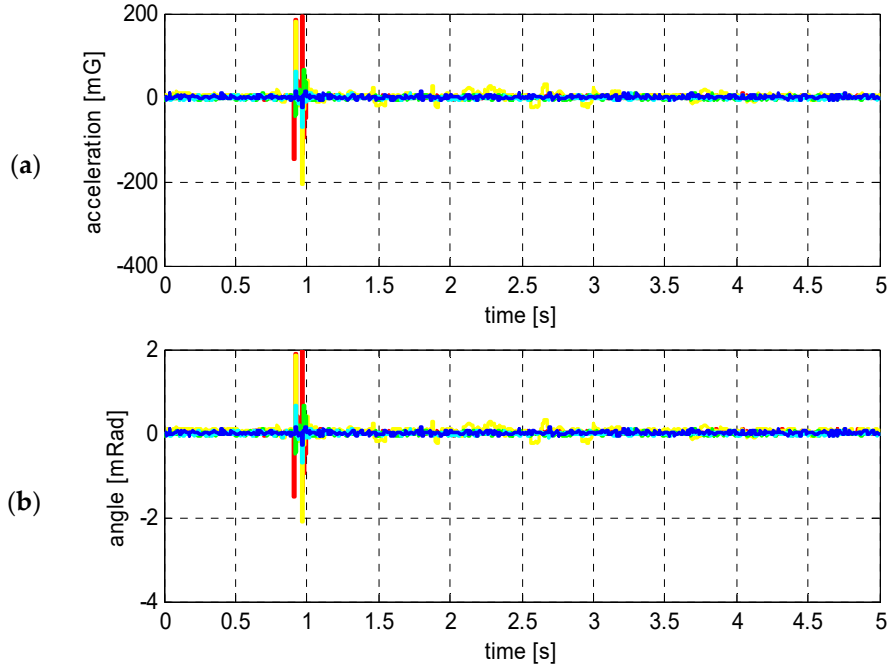

Figure 25. The results of the single impulse test: (**a**) Time–acceleration; (**b**) Time–angle. Material: saclSi 1; Isotropic pressure 20 kPa; Amplitude 8.6 V; Impulse duration 50 ms (– the top sensor, S1, – the second sensor from the top, S2, – the third sensor from the top, S3, – the fourth sensor from the top, S4, – the bottom sensor, S5).

1. Red—the top sensor (S1)
2. Yellow—the second sensor from the top (S2)
3. Green—the third sensor from the top (S3)
4. Cyan—the fourth sensor from the top (S4)
5. Blue—the bottom (fifth) sensor (S5)

3.1. RC Test Results

For sandy soil specimens, the results obtained with the accelerometers attached directly to the specimen comply with the standard RC results. The resonant frequency of the tested specimens was the same in both versions of the test (the frequency corresponding to the largest amplitude in Figures 13–18). However, the tests with the ADXL accelerometers showed some unexpected behavior of the specimens that remained undetected in the standard test version. It can be seen in Figures 13–18 that for certain frequencies there are some anomalies visible on the frequency–angle graph (for example, in Figure 18 at around 100, 150, 165 and 195 Hz). As this kind of behavior occurs around the resonant frequency it can potentially affect the reading.

The same tests were performed on the clayey soil specimens, as those have entirely different characteristics (such specimens behave more like a rigid body compared to the sandy specimens). The resulting resonant frequency was also compliant with the standard RC test result. The vibration phenomena detected in sandy specimens were not present in the clayey ones. However, it can be seen in Figure 22 that the peak value of the rotation angle is not always distinct in the graph resulting from the standard test. The results from the accelerometers were more precise and the peak value can be easily detected, as can the resonant frequency. What is interesting is that on some of the resulting graphs (Figures 20 and 21) the peaks are located differently for each of the accelerometers. It might seem that the bottom sensors respond to a slightly higher frequency than those near the top. However, this could also mean that there was a delay in the wave propagation, as the frequency was measured near the top end of the specimen. Further investigation should be

performed in order to evaluate this hypothesis. There might also be the possibility of using these results as a basis for calculating the wave propagation speed in this type of soil.

It should also be noticed that the bottom part of the specimen (the blue accelerometer) was also moving. In the theoretical description of the RC test there is an assumption that the bottom part is fixed. Therefore, the actual displacement of the top part is the relative displacement of the top part with respect to the displaced bottom part of the specimen, and not to the assumed fixed bottom.

3.2. Single Impulse Test Results

To investigate the phenomena that were detected in the RC tests, the single impulse tests were conducted. The results of the proposed single impulse tests for saclSi soil are presented in Figures 25–27. The same color scheme is adopted as in previous subsection.

The results of the single impulse testing show that the accelerometers do not respond to the excitation in order 1-2-3-4-5 (from the top one to the bottom one). In some tests the bottom one (blue) reacted first. The measurements and readings from the sensors were precisely synchronized, having been taken simultaneously. As the wave speed is known to be higher in materials which the RC device is made of, i.e., metals and polycarbonates, than in soils, the bottom accelerometer could have picked up the signal faster than the middle ones. The observed results suggest that it should be investigated how the vibration of the device equipment affects the results of the standard tests.

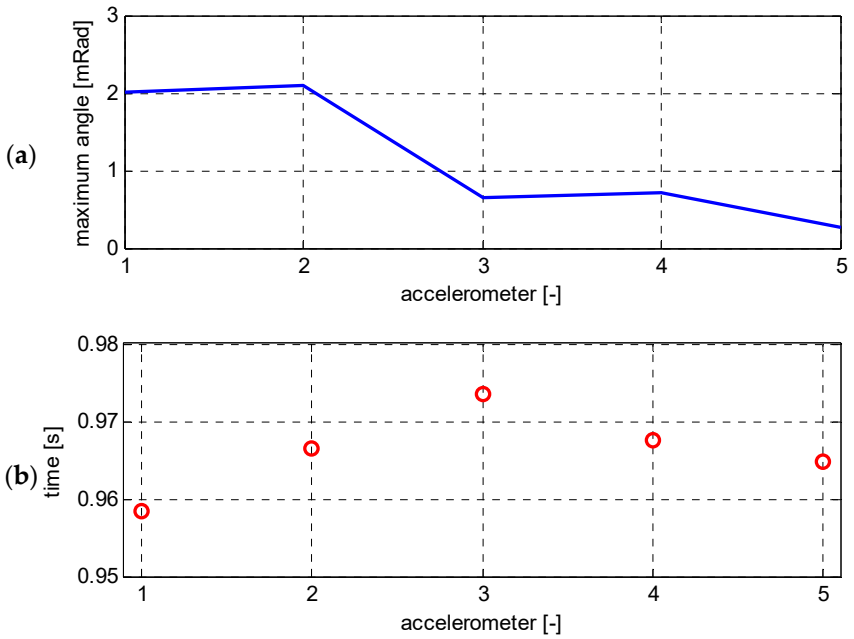

Figure 26. The results of the single impulse test: (**a**) Accelerometer number–maximum angle, (**b**) Accelerometer number–time. Material: saclSi 1; Isotropic pressure 20 kPa; Amplitude 8.6 V; Impulse duration 50 ms.

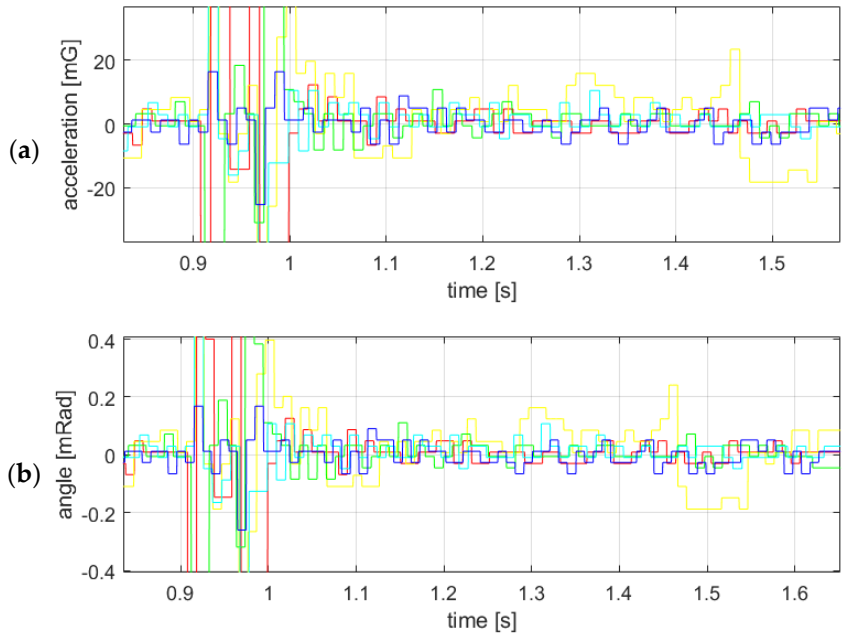

Figure 27. The results of the single impulse test on a larger scale: (**a**) Time–acceleration, (**b**) Time–angle. Material: saclSi 1; Isotropic pressure 20 kPa; Amplitude 8.6 V; Impulse duration 50 ms (– the top sensor, S1, – the second sensor from the top, S2, – the third sensor from the top, S3, – the fourth sensor from the top, S4, – the bottom sensor, S5).

4. Discussion

The additional accelerometers attached to the specimen's surface allowed observation of the material's reaction to the applied loading in several different regions of the specimen.

1. In cohesionless soil specimens (Figures 13–18 and Figure 28a left) the rotation amplitude decreases with the distance to the vibration source (the drive system). This observation is compliant with the commonly used theoretical description of the RC test results.
2. In cohesive soil samples, the rotation amplitude measured with the bottom accelerometer (blue) is noticeably larger than the differences in amplitudes measured with subsequent accelerometers (cyan, green, yellow and red), suggesting that the bottom part of the sample cannot be considered fixed as is commonly assumed. It is very likely that the bottom part of the sample slips over the porous stone supporting the sample (see Figure 28b left). A similar phenomenon has been observed when [41] using an optical measuring method for cyclic slow-changing torsional shearing tests of clayey samples. This indicates that the original RC/TS device construction might not be appropriate in such cases. Therefore, other techniques should be used to ensure that the bottom is fixed. It should also be noted that the ASTM standard [42] does not consider the occurrence of this phenomenon. The observed effect influences the determination of soil parameters, so it should not be neglected.

The measurements taken with the accelerometers directly attached to the surface of the specimens and not to the drive system allowed for substantial noise reduction and elimination of signal corruption in tests performed on sandy soil (see Figures 19–22 in the 180–210 Hz range). It should be noted that the second amplitude peak is present only in results obtained with the proximity sensors, and might be caused by interference from waves generated by the drive system and the reflection of these waves from other elements of the device. The results obtained with the additional accelerometers are not affected by this kind of disturbance, so the proposed modified method should be a more reliable basis for determination of the mechanical parameters of soil.

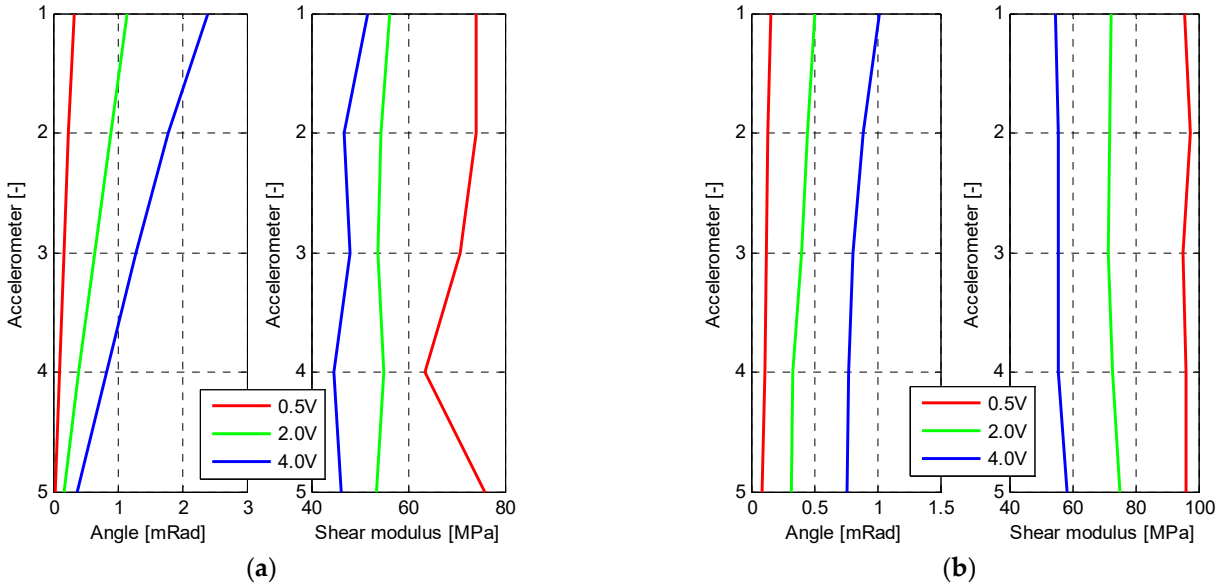

Figure 28. The shear modulus and maximum angle of rotation along the height of the soil sample (isotropic pressure 50 kPa): (**a**) Material: Sa 3; (**b**) Material: saclSi 1.

The sandy soil test results (Figures 13–18) show some disturbances of the vibration pattern localized around certain frequencies (multiples of 50 Hz: 50, 100, 150 and 200 Hz). The effect could be caused by the interference of the emitted wave and the wave reflected from the bottom surface of the specimen. On the other hand, some disturbances might be caused by the accelerometers themselves; to be more specific, the inertia of the accelerometers should be considered as a factor. However, further experiments need to be conducted in order to evaluate these hypotheses.

The very complex structure of the power spectral density of registered signals is a consequence of the observed disturbances (see Figures 29 and 30). In the case of sand Sa 3 subjected to isotropic pressure of 50 kPa, interpretation of the G modulus is possible, but determination of the damping ratio D is very uncertain. In sand Sa 3 subjected to an isotropic pressure of 100 kPa, both the G and D values cannot be interpreted because of the irregular fluctuations in the recorded signal. It should be noted that in the tests carried out on samples of cohesive soils (saclSi 1), such effects were not found, and the interpretation of the results gave unambiguous G and D values (see Figures 28, 31 and 32 and Table 2). This may lead to the conclusion that dry non-cohesive soils, forming a group of grains that interact with each other mainly through frictional forces, may behave in a more complex manner than is assumed in the standardized test method during dynamic loading. There is a probability that the observable disturbances of vibrations represent a local reaction of the granular soil to the applied loads. This issue requires further research with the use of measuring techniques that would allow for locally focused observations both on the surface and inside of the sample.

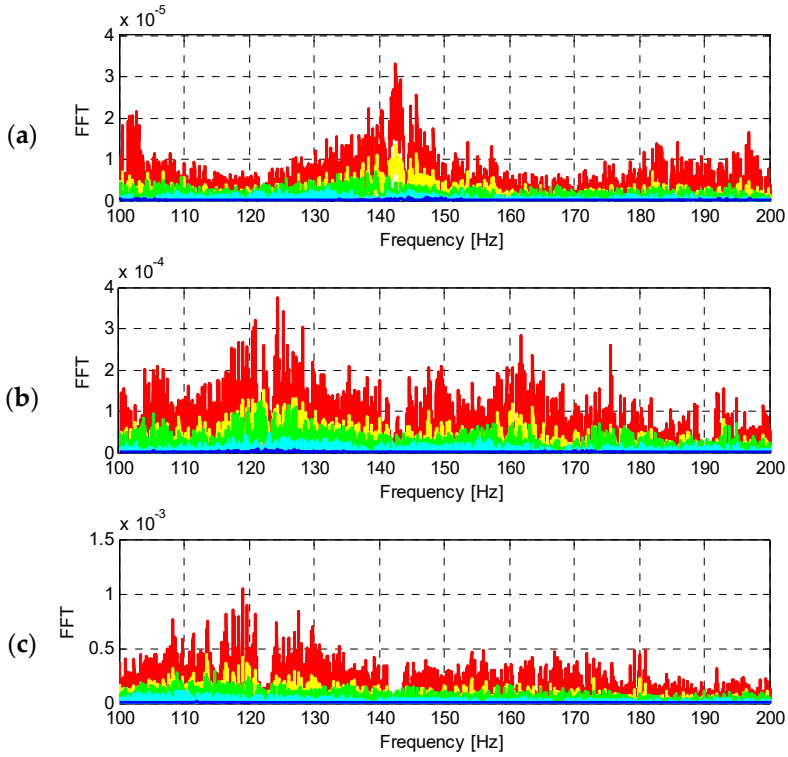

Figure 29. Power spectral density of the results from the additional accelerometers. Material: Sa 3; Isotropic pressure 50 kPa; Frequency spectrum 100–200 Hz; Excitation (torque) amplitude: (**a**) 0.5 V, (**b**) 2 V, (**c**) 4 V (– the top sensor, S1, – the second sensor from the top, S2, – the third sensor from the top, S3, – the fourth sensor from the top, S4, – the bottom sensor, S5).

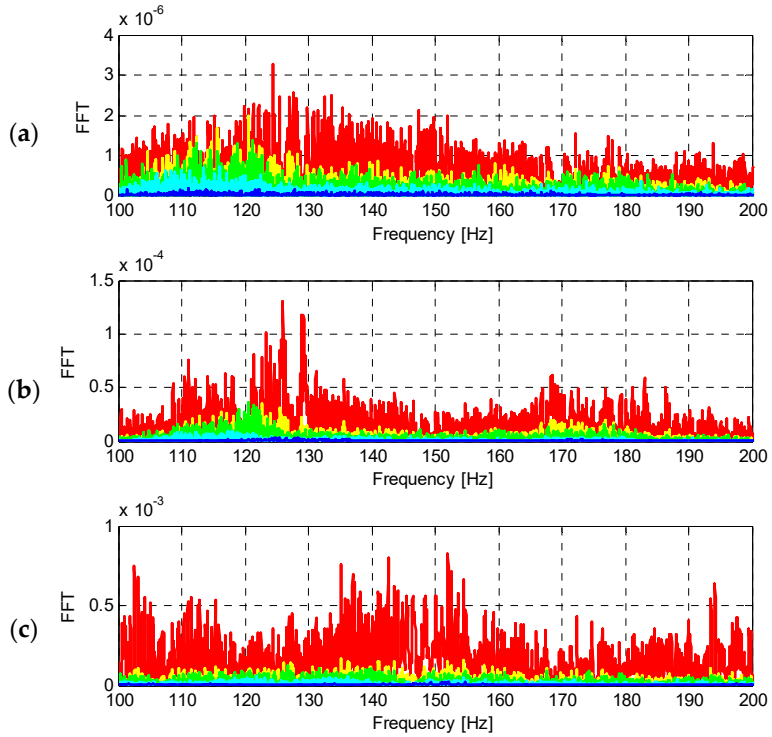

Figure 30. Power spectral density of the results from the additional accelerometers. Material: Sa 3; Isotropic pressure 100 kPa; Frequency spectrum 100–220 Hz; Excitation (torque) amplitude: (**a**) 0.5 V, (**b**) 2 V, (**c**) 4 V (– the top sensor, S1, – the second sensor from the top, S2, – the third sensor from the top, S3, – the fourth sensor from the top, S4, – the bottom sensor, S5).

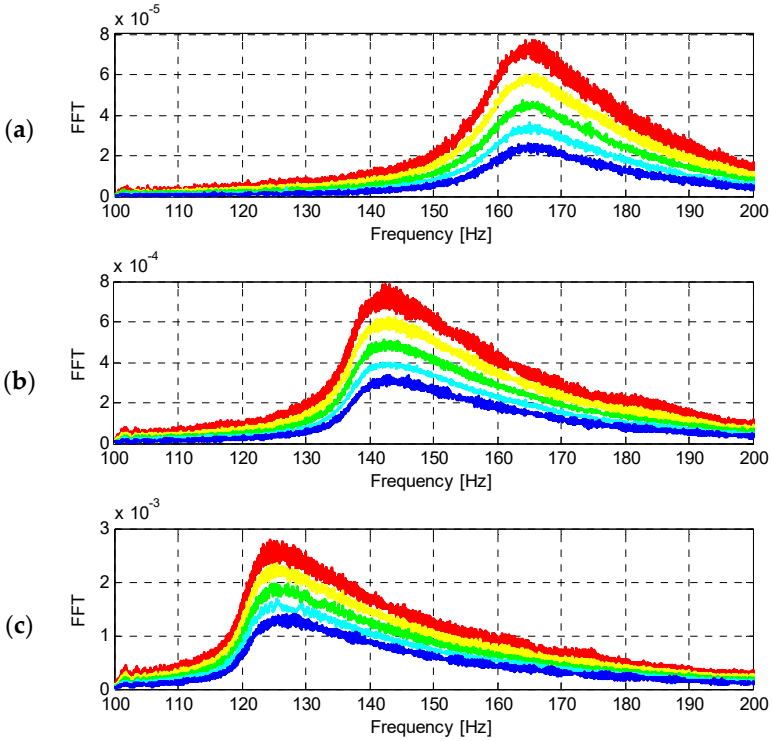

Figure 31. Power spectral density of the results from the additional accelerometers. Material: saclSi 1; Isotropic pressure 50 kPa; Frequency spectrum 100–250 Hz; Excitation (torque) amplitude: (**a**) 0.5 V, (**b**) 2 V, (**c**) 4 V (– the top sensor, S1, – the second sensor from the top, S2, – the third sensor from the top, S3, – the fourth sensor from the top, S4, – the bottom sensor, S5).

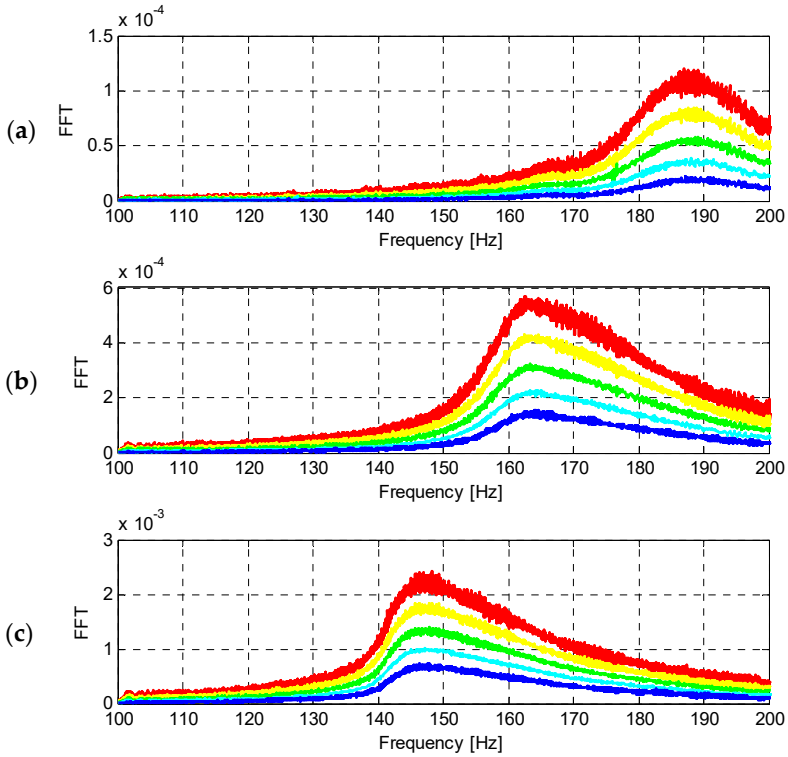

Figure 32. Power spectral density of the results from the additional accelerometers. Material: saclSi 1; Isotropic pressure 100 kPa; Frequency spectrum 100–250 Hz; Excitation (torque) amplitude: (**a**) 0.5 V, (**b**) 2 V, (**c**) 4 V (– the top sensor, S1, – the second sensor from the top, S2, – the third sensor from the top, S3, – the fourth sensor from the top, S4, – the bottom sensor, S5).

Table 2. Comparison of the obtained results [1].

Soil Type	p [kPa]	Excitation [V]	Built-In Sensor			Accelerometers		
			f_r [Hz]	G [MPa]	D [%]	f_r [Hz]	G [MPa]	D [%]
Sa 3	50	0.5	150.33	80.00	3.04	146.07	71.65	3.57 *
		2.0	125.09	55.29	3.33	127.71	54.61	4.69 *
		4.0	103.36	37.81	6.37	118.90	47.44	2.41 *
	100	0.5	193.18	131.86	2.73	**	**	**
		2.0	170.72	103.28	7.28	**	**	**
		4.0	152.04	81.78	4.78	**	**	**
saclSi 1	50	0.5	163.94	100.09	5.65	165.01	96.06	7.27
		2.0	141.24	74.19	7.70	143.68	72.76	9.05
		5.0	124.30	57.64	8.31	125.90	56.04	10.52
	100	0.5	197.39	144.92	6.60	188.09	124.64	6.51
		2.0	163.64	99.62	7.40	163.47	94.21	9.02
		5.0	145.60	78.83	7.68	147.87	77.03	8.45

[1] p—isotropic pressure, f_r—resonant frequency, G—shear modulus, D—damping ratio; * the interpretation is not unequivocal due to significant signal distortion; ** the signal distortion is too high to be reliably interpreted.

The proposed single impulse method (Figure 25) allowed observation of the propagation of a mechanical wave in the specimens. The signal measured by the accelerometers (Figures 26 and 27) was complex, which was probably caused by numerous refractions and interferences from mechanical waves traveling through the specimen. The conducted study did not allow for description of a relation between the generated impulses and the signal picked up by the accelerometers. Therefore, additional studies will be conducted in the future.

5. Conclusions

In this study, a modified version of a dynamic soil test in a Resonant Column was proposed. The modified RC device and additional testing procedure (single impulse technique) allowed observation of some dynamic phenomena that remained undetected in the standard tests.

1. In sandy soil specimens, some irregularities can be noticed on the frequency-angle graph resulting from the RC test. The abnormalities occur for certain frequencies and are observable only for cohesionless soil. It should be investigated whether this was due to the soil or the characteristics of the testing equipment.
2. In clayey soils, the proposed measurement method proved to be more accurate. In standard RC testing the peak value of the rotation angle is not always distinct; thus, it can be difficult to determine the resonant frequency correctly. This issue can be solved using accelerometers attached directly to the surface of the specimen in order to avoid detecting the resonance of device equipment.
3. In some cohesive soil specimens, the readings from individual accelerometers could potentially be used for calculating the wave propagation speed in the soil material, as there was an observable delay in the occurrence of peaks visible on the time–angle graph.
4. The proposed single impulse test showed that the fact that the wave propagation speed is higher through the elements of device equipment can have an impact on the behavior of the specimens. The accelerometers did not react in order, from closest-to-the-source to farthest-to-source; rather, in some cases the lowest sensor picked up the signal faster than the middle ones. This effect should be studied further in order to evaluate the possibility of transmitted wave interaction (interference, refraction or standing wave occurrence).
5. The values of the shear modulus G obtained from the tests with the use of the original and new measuring systems are very similar to each other. The average value of the relative differences does not exceed 8%; taking into account the safety margins required by soil dynamic testing standards (10%), this can be treated as a

satisfactory result. In the case of the damping ratio D, the mean spread is much larger (25%). Nevertheless, the variability of the G and D values along the height of the tested samples is certainly valuable information, and could be especially useful for examination of local properties resulting from the influence of soil heterogeneity, lamination and stratification.

The proper determination of soil stiffness and dynamic parameters is crucial for foundation design, especially for the structures subjected to complex dynamic and cyclic loading conditions such as offshore wind turbines. Therefore, the laboratory methods for soil testing should be constantly reevaluated and developed. The authors aim to conduct a thorough investigation of the hypotheses formulated based on these results and to further examine the observed phenomena.

Author Contributions: Conceptualization, P.E.S., M.B. (Marcin Bujko) and I.D.; methodology, P.E.S.; software, P.E.S.; validation, I.D., M.B. (Marcin Bujko) and M.B. (Marta Bocheńska); formal analysis, M.B. (Marta Bocheńska); investigation, P.E.S., I.D. and M.B. (Marcin Bujko); resources, P.E.S., I.D., M.B. (Marcin Bujko) and M.B. (Marta Bocheńska); data curation, M.B. (Marcin Bujko); writing—original draft preparation, M.B. (Marta Bocheńska); writing—review and editing, P.E.S. and M.B. (Marcin Bujko); visualization, M.B. (Marta Bocheńska) and I.D.; supervision, P.E.S.; project administration, P.E.S. and I.D. All authors have read and agreed to the published version of the manuscript.

Funding: This research received no external funding.

Institutional Review Board Statement: Not applicable.

Informed Consent Statement: Not applicable.

Data Availability Statement: The data that support the findings of this study are available from the corresponding author, [M.B. (Marta Bocheńska)], upon reasonable request.

Conflicts of Interest: The authors declare no conflict of interest.

References

1. Global Wind Energy Council. Global Wind Report 2021. 24 March 2021. Available online: https://gwec.net/global-wind-report-2021 (accessed on 11 August 2021).
2. IRENA. *Renewable Capacity Statistics 2021*; International Renewable Energy Agency (IRENA): Abu Dhabi, United Arab Emirates, 2021; Available online: https://www.irena.org/publications/2021/March/Renewable-Capacity-Statistics-2021 (accessed on 11 August 2021).
3. Wei, X.; Duan, Y.; Liu, Y.; Jin, S.; Sun, C. Onshore-offshore wind energy resource evaluation based on synergetic use of multiple satellite data and meteorological stations in Jiangsu Province, China. *Front. Earth Sci.* **2019**, *13*, 132–150. [CrossRef]
4. Byrne, B.; Houlsby, G. Foundations for offshore wind turbines. *Philos. Trans. R. Soc. Lond. Ser. A Math. Phys. Eng. Sci.* **2003**, *361*, 2909–2930. [CrossRef]
5. Houlsby, G.T.; Ibsen, L.B.; Byrne, B.W. Suction caissons for wind turbines. In *Frontiers in Offshore Geotechnics*; ISFOG: Perth, WA, Australia, 2005; pp. 75–93.
6. Houlsby, G.; Kelly, R.; Huxtable, J.; Byrne, B. Field trials of suction caissons in clay for offshore wind turbine foundations. *Géotechnique* **2005**, *55*, 287–296. [CrossRef]
7. Wu, X.; Hu, Y.; Li, Y.; Yang, J.; Duan, L.; Wang, T.; Adcock, T.; Jiang, Z.; Gao, Z.; Lin, Z.; et al. Foundations of offshore wind turbines: A review. *Renew. Sustain. Energy Rev.* **2019**, *104*, 379–393. [CrossRef]
8. Iliopoulos, A.; Weijtjens, W.; Van Hemelrijck, D.; Devriendt, C. Fatigue assessment of offshore wind turbines on monopile foundations using multi-band modal expansion. *Wind Energy* **2017**, *20*, 1463–1479. [CrossRef]
9. Staubach, P.; Wichtmann, T. Long-term deformations of monopile foundations for offshore wind turbines studied with a high-cycle accumulation model. *Comput. Geotech.* **2020**, *124*, 103553. [CrossRef]
10. Zachert, H.; Wichtmann, T.; Kudella, P.; Triantafyllidis, T. Inspection of a high-cycle accumulation model for sand based on recalculations of a full-scale test on a gravity base foundation for offshore wind turbines. *Comput. Geotech.* **2020**, *126*, 103727. [CrossRef]
11. Pavlou, D.G. Soil–Structure–Wave Interaction of Gravity-Based Offshore Wind Turbines: An Analytical Model. ASME. *J. Offshore Mech. Arct. Eng.* **2021**, *143*, 032101. [CrossRef]
12. Ma, H.; Yang, J.; Chen, L. Effect of scour on the structural response of an offshore wind turbine supported on tripod foundation. *Appl. Ocean Res.* **2018**, *73*, 179–189. [CrossRef]
13. Liang, F.; Zheng, H.; Zhang, H. On the pile tension capacity of scoured tripod foundation supporting offshore wind turbines. *Appl. Ocean Res.* **2020**, *102*, 102323. [CrossRef]

14. Jeong, Y.-H.; Kim, J.-H.; Park, H.-J.; Kim, D.-S. Cyclic behavior of unit bucket for tripod foundation system supporting offshore wind turbine via model tests. *Wind Energy* **2019**, *22*, 257–268. [CrossRef]
15. Ko, Y.-Y.; Li, Y.-T. Response of a scale-model pile group for a jacket foundation of an offshore wind turbine in liquefiable ground during shaking table tests. *Earthq. Eng. Struct. Dyn.* **2020**, *49*, 1682–1701. [CrossRef]
16. Shittu, A.A.; Mehmanparast, A.; Hart, P.; Kolios, A. Comparative study between S-N and fracture mechanics approach on reliability assessment of offshore wind turbine jacket foundations. *Reliab. Eng. Syst. Saf.* **2021**, *215*, 107838. [CrossRef]
17. Kong, D.; Wen, K.; Zhu, B.; Zhu, Z.; Chen, Y. Centrifuge Modeling of Cyclic Lateral Behaviors of a Tetrapod Piled Jacket Foundation for Offshore Wind Turbines in Sand. *J. Geotech. Geoenviron.* **2019**, *145*, 04019099. [CrossRef]
18. Wang, X.; Zeng, X.; Li, J. Vertical performance of suction bucket foundation for offshore wind turbines in sand. *Ocean Eng.* **2019**, *180*, 40–48. [CrossRef]
19. Skau, K.S.; Grimstad, G.; Page, A.M.; Eiksund, G.R.; Jostad, H.P. A macro-element for integrated time domain analyses representing bucket foundations for offshore wind turbines. *Mar. Struct.* **2018**, *59*, 158–178. [CrossRef]
20. Ding, H.; Hu, R.; Zhang, P.; Le, C. Load bearing behaviors of composite bucket foundations for offshore wind turbines on layered soil under combined loading. *Ocean Eng.* **2020**, *198*, 106997. [CrossRef]
21. Li, H.; Soares, C.G.; Huang, H.-Z. Reliability analysis of a floating offshore wind turbine using Bayesian Networks. *Ocean Eng.* **2020**, *217*, 107827. [CrossRef]
22. Li, H.; Díaz, H.; Soares, C.G. A failure analysis of floating offshore wind turbines using AHP-FMEA methodology. *Ocean Eng.* **2021**, *234*, 109261. [CrossRef]
23. Li, H.; Diaz, H.; Soares, C.G. A developed failure mode and effect analysis for floating offshore wind turbine support structures. *Renew. Energy* **2021**, *164*, 133–145. [CrossRef]
24. Chen, D.; Gao, P.; Huang, S.; Li, C.; Yu, X. Static and dynamic loading behavior of a hybrid foundation for offshore wind turbines. *Mar. Struct.* **2020**, *71*, 102727. [CrossRef]
25. Wang, X.; Zeng, X.; Yang, X.; Li, J. Feasibility study of offshore wind turbines with hybrid monopile foundation based on centrifuge modeling. *Appl. Energy* **2018**, *209*, 127–139. [CrossRef]
26. Wang, X.; Zeng, X.; Li, J.; Yang, X. Lateral bearing capacity of hybrid monopile-friction wheel foundation for offshore wind turbines by centrifuge modelling. *Ocean Eng.* **2018**, *148*, 182–192. [CrossRef]
27. Ma, H.; Yang, J. A novel hybrid monopile foundation for offshore wind turbines. *Ocean Eng.* **2020**, *198*, 106963. [CrossRef]
28. Wang, X.; Zeng, X.; Li, J.; Yang, X.; Wang, H. A review on recent advancements of substructures for offshore wind turbines. *Energy Convers. Manag.* **2018**, *158*, 103–119. [CrossRef]
29. Srokosz, P.E.; Dyka, I.; Bujko, M. Determination of shear modulus of soil in the RC/TS apparatus for designing offshore wind power plant foundations. *Pol. Marit. Res.* **2018**, *25*, 69–83. [CrossRef]
30. Futai, M.M.; Haigh, S.K.; Madabhushi, G.S.P. Comparison of the dynamic responses of monopiles and gravity base foundations for offshore wind turbines in sand using centrifuge modelling. *Soils Found.* **2020**, *61*, 50–63. [CrossRef]
31. Zuo, H.; Bi, K.; Hao, H. Dynamic analyses of operating offshore wind turbines including soil-structure interaction. *Eng. Struct.* **2018**, *157*, 42–62. [CrossRef]
32. Abhinav, K.A.; Saha, N. Nonlinear dynamical behaviour of jacket supported offshore wind turbines in loose sand. *Mar. Struct.* **2018**, *57*, 133–151. [CrossRef]
33. Bhattacharya, S.; Nikitas, G.; Vimalan, N. Dynamic SSI of Monopile-Supported Offshore Wind Turbines. In *Geotechnical Design and Practice*; Ilamparuthi, K., Robinson, R., Eds.; Developments in Geotechnical Engineering; Springer: Singapore, 2019; pp. 113–123. [CrossRef]
34. Skau, K.S.; Jostad, H.P.; Eiksund, G.; Sturm, H. Modelling of soil-structure-interaction for flexible caissons for offshore wind turbines. *Ocean Eng.* **2019**, *171*, 273–285. [CrossRef]
35. Arany, L.; Bhattacharya, S.; Macdonald, J.; Hogan, S.J. Design of monopiles for offshore wind turbines in 10 steps. *Soil Dyn. Earthq. Eng.* **2017**, *92*, 126–152. [CrossRef]
36. Srokosz, P.E.; Bujko, M.; Bocheńska, M.; Ossowski, R. Optical flow method for measuring deformation of soil specimen subjected to torsional shearing. *Measurement* **2021**, *174*, 109064. [CrossRef]
37. ISO 14688-1:2002, Geotechnical Investigation and Testing—Identification and Classification of Soil—Part 1: Identification and Description. Available online: https://www.iso.org/standard/25260.html (accessed on 7 October 2021).
38. Wichtmann, T. Soil Behaviour under Cyclic Loading—Experimental Observations, Constitutive Description and Applications. Habilitation Thesis, Karlsruhe Institute of Technology, Karlsruhe, Baden-Wuerttemberg, Germany, 2016.
39. Dyka, I.; Srokosz, P.E.; Bujko, M. Influence of grain size distribution on dynamic shear modulus of sands. *Open Eng.* **2017**, *7*, 317–329. [CrossRef]
40. Srokosz, P.E.; Dyka, I.; Bujko, M. *Badania Sztywności Gruntu w Kolumnie Rezonansowej*; Monograph, Wydawnictwo Uniwersytetu Warmińsko-Mazurskiego w Olsztynie: Olsztyn, Poland, 2017.
41. Bujko, M.; Srokosz, P.E.; Dyka, I. Use of optical method for improvement of soil dynamic tests in torsional shear apparatus. In Proceedings of the 2017 Baltic Geodetic Congress (BGC Geomatics), Gdansk, Poland, 22–25 June 2017; pp. 404–408. [CrossRef]
42. *ASTM Standard D4015—92, Standard Test Methods for Modulus and Damping of Soils by the Resonant-Column Method*; ASTM International: West Conshohocken, PA, USA, 2000.